Journal of Sound and Vibration (2001) **244**(1), 57–77
doi:10.1006/jsvi.2000.3458, available online at http://www.idealibrary.com on IDEAL®

AEROACOUSTIC RESPONSE OF A SLIT-SHAPED DIAPHRAGM IN A PIPE AT LOW HELMHOLTZ NUMBER, 2: UNSTEADY RESULTS

G. C. J. Hofmans

Fluid Dynamics Laboratory, Faculty of Applied Physics, Eindhoven University of Technology, Postbus 513, 5600 *MB Eindhoven, The Netherlands*

M. Ranucci

University 'La Sapienza', Dipartimento Di Meccanica E Aeronautica, Via Eudossiana 18, 00184, *Rome, Italy*

G. Ajello and Y. Auregan

*Laboratoire d'Acoustique, Université du Maine Av. Olivier Messiaen BP*535, 72017 *Le Mans, France*

and

A. Hirschberg

Fluid Dynamics Laboratory, Faculty of Applied Physics, Eindhoven University of Technology, Postbus 513, 5600 *MB Eindhoven, The Netherlands. E-mail: a.hirschberg@phys.tue.nl*

(*Received* 18 *October* 1999, *and in final form* 18 *October* 2000)

In a companion paper the quasi-steady aeroacoustic behavior of diaphragms which prevails for low Strouhal number but Mach number of order unity was discussed. The complementary case of a small Mach number and a Strouhal number of order unity is now considered. In this case, a two-dimensional numerical method is used to predict the Strouhal-number dependence of the coefficients of the scattering matrix. The numerical method solves the two-dimensional incompressible flow equations by means of the vortex-blob method. The quality of the numerical results is investigated by comparing results of Howe's energy formulation with results obtained by an integral formulation to calculate the pressure difference across the diaphragm. The predictions of the coefficients are compared with experimental measurements carried out at LAUM. It is shown that the low- and high-frequency behavior are quite well predicted, while for intermediate frequencies a deviation between numerical simulations and experimental measurements is observed. While this is not yet fully understood it is expected to be related to whistling induced by the finite thickness of the diaphragm in the experiments.

1. INTRODUCTION

For some aeroacoustic problems it is possible to separate the flow domain into a region of wave propagation and an acoustic source region. When the dimensions of the source region are small compared to the wavelength of the acoustic perturbation ($He \ll 1$), the source region can be considered compact. There are two reasons for the source region to be considered compact: i.e., (1) the local flow in the source region can be considered

0022-460X/01/260057 + 21 $35.00/0

quasi-steady, or (2) the local flow in the source region can be considered incompressible. In the first case, the acoustic source can be described by a quasi-steady model even taking compressibility effects into account as was done in the companion paper [1]. In the second case, the unsteady incompressible flow equations have to be solved. It is usually necessary to solve these equations numerically when considering arbitrary amplitudes. In the case of linear perturbations, an analytical model has been proposed by Howe [2] which has been used by Dowling and Hughes [3] and more recently by Wendoloski [4].

For low-Mach-number isentropic flows unsteady vorticity is the main source of sound. Therefore one can restrict oneself to solving the flow in the source region accurately describing the development of the vorticity field in the incompressible flow limit. Furthermore, only source regions for which a two-dimensional description is reasonable are considered.

In order to model the high-frequency response of a slit-shaped diaphragm in a pipe, a numerical method is used to simulate the flow. It yields a solution of the two-dimensional frictionless incompressible flow equations and it includes flow separation at the edges of the diaphragm described by a Kutta condition. Because the method is an incompressible flow method, the results can only be applied to compact low-Mach-number flows. Results such as the acoustic losses due to the flow through the diaphragm, are presented. A comparison is made between two different formulations of the acoustic source power; results of Howe's energy formulation [5] for the acoustic source power are compared with results of an integral formulation for the pressure using the Green function. The acoustic power is studied as a function of acoustic amplitude and diaphragm opening. Also, the influence of some details of the geometry of the diaphragm is studied. Another result of this method is the acoustic source pressure Δp_{source} that can be incorporated in an acoustic model of the diaphragm flow. The acoustic pressures upstream of the diaphragm and the acoustic pressures downstream of the diaphragm are related by the so-called scattering matrix [6]. Predictions of the components of the scattering matrix are compared to low-Mach-number high-frequency experimental results obtained by means of a two-source method.

2. NUMERICAL METHOD

2.1. VORTICITY–TRANSPORT EQUATION

The dynamics of incompressible two-dimensional flows are governed by the conservation of mass and momentum, which in non-dimensional form upon choosing a reference length L_{ref} and a reference velocity U_{ref}, have the following forms: mass conservation equation,

$$\nabla \cdot \mathbf{u} = 0, \tag{1}$$

momentum equation,

$$\frac{\partial \mathbf{u}}{\partial t} - \omega \mathbf{u}^{\perp} = -\nabla\left(p + \frac{|u|^2}{2}\right) + \frac{1}{\mathrm{Re}}\nabla^{\perp}\omega. \tag{2}$$

Here ω is the vorticity, $\mathbf{u}^{\perp} = (-u_2, u_1)$ is the velocity vector rotated over 90°, and $\nabla^{\perp} = (-\partial/\partial x_2, \partial/\partial x_1)$ is the gradient operator rotated over 90°. In a two-dimensional flow the only non-zero component of the vorticity is directed along the third dimension, hence $\boldsymbol{\omega} = (0, 0, \omega)$. Note that the density ρ drops out due to the scaling of the equation; nevertheless, it is present in the scaling of the pressure with ρU_{ref}^2. The vorticity–transport

equation is derived by taking the curl of the momentum equation (2):

$$\frac{\partial \omega}{\partial t} + \mathbf{u} \cdot \nabla \omega = \frac{1}{\mathrm{Re}} \nabla^2 \omega. \tag{3}$$

In this equation one can recognize the two processes that change the vorticity distribution. The first process is the inviscid advection of vorticity described by the advection equation:

$$\mathrm{D}\omega/\mathrm{D}t = 0, \tag{4}$$

in which $\mathrm{D}/\mathrm{D}t$ is the material derivative defined as, $\mathrm{D}/\mathrm{D}t = \partial/\partial t + \mathbf{u} \cdot \nabla$. The second process is the diffusion of vorticity described by

$$\frac{\partial \omega}{\partial t} = \frac{1}{\mathrm{Re}} \nabla^2 \omega. \tag{5}$$

At high Reynolds number the process of diffusion has only a small effect on the evolution of distributed vorticity. In that case the transport of vorticity is governed by the advection equation (4). In a subsequent section a desingularized point-vortex method is presented to solve the vorticity–transport equation, while neglecting diffusion (see also references [7, 8]). In the subsequent part of this paper the method is referred to as "the vortex-blob" method.

One can choose to solve numerically the vorticity–transport equation, as opposed to the Navier–Stokes equations for the primitive variable $\mathbf{u}$. The velocity field is obtained from the distribution of vorticity and also the pressure field is available through the integral formulation that is presented in the next section. By solving the vorticity–transport equation the computational effort can be focused on the regions of the flow domain where vorticity is present. At high Reynolds numbers vorticity is restricted to thin shear layers as a result of flow separation. This flow separation is described at sharp edges by assuming a tangential separation of the flow, which corresponds to the so-called Kutta condition for frictionless flows.

2.2. VORTEX-BLOB METHOD FOR INVISCID FLOW

When considering the transport of vorticity in a fixed two-dimensional domain Ω enclosed by a contour $\partial\Omega$ the velocity field is given by

$$\mathbf{u}(\mathbf{x}, t) = \int_{\partial\Omega} u_n \mathbf{K}^{\perp}(\mathbf{x} - \mathbf{y})\, \mathrm{d}s(\mathbf{y}) - \int_{\partial\Omega} u_\tau \mathbf{K}(\mathbf{x} - \mathbf{y})\, \mathrm{d}s(\mathbf{y}) + \iint_{\Omega} \omega \mathbf{K}(\mathbf{x} - \mathbf{y})\, \mathrm{d}\Omega(\mathbf{y}), \tag{6}$$

where $\mathbf{K}(\mathbf{x})$ is the Biot–Savart kernel

$$\mathbf{K}(\mathbf{x}) = \frac{1}{2\pi} \frac{\mathbf{x}^{\perp}}{|\mathbf{x}|^2}, \quad \mathbf{x}^{\perp} = (-x_2, x_1).$$

The unit tangential vector $\boldsymbol{\tau}$ along the boundary is defined in an anti-clockwise direction (with the fluid domain on the left) orthogonal to the unit normal vector that is directed outwards: $\boldsymbol{\tau} = \mathbf{n}^{\perp}$ (see Figure 1). The velocity field has to satisfy only one boundary condition on the solid walls in the domain: $u_n = 0$. On the inflow section of the domain the uniform inflow velocity u_{in} is prescribed: $u_n = -u_{in}(t)$. On the outflow section of the domain the uniform outflow velocity u_n follows through mass conservation from the inflow velocity.

The vorticity field ω is approximated by a set of point vortices,

$$\omega = (\mathbf{x}, t) = \sum_{j=1}^{N} \Gamma_j \delta(\mathbf{x} - \mathbf{x}_j),$$

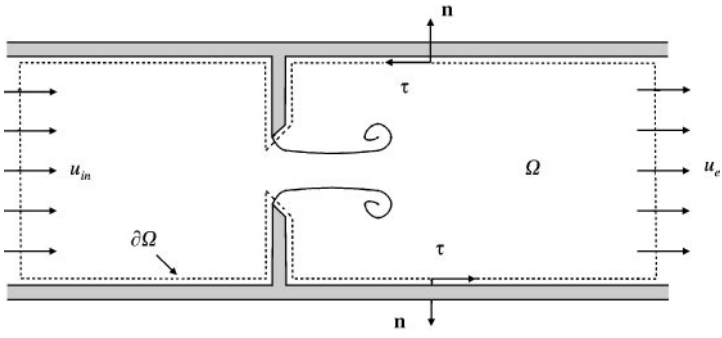

Figure 1. Definition of the integration domain and the unit vectors in the case of a diaphragm in a straight pipe.

in which Γ_j is the constant circulation of the jth point vortex at position $\mathbf{x}_j$ and $\delta(\mathbf{x} - \mathbf{x}_j)$ is the Dirac delta function. The positions of the individual vortices change in time according to

$$\mathrm{d}\mathbf{x}_j/\mathrm{d}t = \mathbf{u}(\mathbf{x}_j, t). \tag{7}$$

In the absence of solid walls in the flow domain the velocity is completely determined by the vorticity distribution. This leads to the following result for the velocity field:

$$\mathbf{u}(\mathbf{x}, t) = \sum_{j=1}^{N} \mathbf{K}(\mathbf{x} - \mathbf{x}_j)\Gamma_j. \tag{8}$$

When $\mathbf{x} = \mathbf{x}_j$ the above relation gives a singular value for the velocity at the jth vortex: It has been shown that ignoring this contribution leads to a correct approximation of the continuous velocity field, see reference [9]; i.e., each vortex has to move as if convected by the net velocity field of all the other vortices. Moreover, the numerical evaluation of the convolution (8) can be affected by large inaccuracies as $\mathbf{x} \to \mathbf{x}_j$. Two point vortices can be so close that their mutual interaction is diverging as the inverse $1/r$ of the distance r between these point vortices. This causes the development of a singularity in the solution at finite time, the effect of which can be removed only by solving the system (7) with an arbitrarily small time step.

In the literature several approaches have been made to regularize the solution. Chorin and Bernard [10] suggested the adoption of a regular vorticity field, with finite-core vortices (blobs) instead of the Dirac delta function. The convolution with the singular Biot–Savart kernel produces a new modified kernel for the velocity representation (8). A better approximation of the solution is obtained even if the dynamics of these vortices is only approximately a solution of the original equations. In fact, the vorticity distribution of each blob, and therefore its shape, is fixed in time upon ignoring the action of the local strain field on the vorticity field.

Beale and Majda [11] proved the accuracy, the linear stability and the convergence of this model for the solution of the original equations. They proposed the following desingularized kernel:

$$\mathbf{K}_\delta(\mathbf{x}) = \mathbf{K}(\mathbf{x})(1 - \exp(-|\mathbf{x}|^2/\delta_v^2)). \tag{9}$$

In this equation δ_v is the so-called desingularization parameter. The contribution to the vorticity distribution of the jth vortex associated with this vortex blob is

$$\omega_j(\mathbf{x}) = \frac{\Gamma_j}{2\pi}\frac{2}{\delta_v^2}\exp(-|\mathbf{x} - \mathbf{x}_j|^2/\delta_v^2), \tag{10}$$

which is a Gaussian distribution. An alternative kernel was proposed by Krasny [12–14]:

$$\mathbf{K}_\delta(\mathbf{x}) = \mathbf{K}(\mathbf{x}) \cdot \frac{|\mathbf{x}|^2}{|\mathbf{x}|^2 + \delta_v^2}. \tag{11}$$

The vorticity distribution associated with this kernel is

$$\omega_j(\mathbf{x}) = \frac{\Gamma_j}{2\pi} \cdot \frac{2\delta_v^2}{(|\mathbf{x} - \mathbf{x}_j|^2 + \delta_v^2)^2}. \tag{12}$$

The value of δ_v in equations (9) and (11) determines the level of desingularization. Although these desingularization kernels are significantly different, it has been shown that the influence of the exact form of the kernels on the numerical result is much less important than the value of δ_v: comparable values of δ_v with different forms of the desingularization kernel lead to very similar results for the kind of problems of interest here, as shown by Hofmans *et al.* [15]. However, note that both equations (10) and (12) indicate that the vorticity distribution is not localized to the immediate neighborhood of $\mathbf{x} = \mathbf{x}_j$ but rather spreads out to infinity.

In the presence of solid boundaries the tangential velocity along the boundaries of the domain is obtained from the projection of equation (6) along the local tangent: i.e., for a point $\mathbf{x}$ on $\partial\Omega$,

$$\frac{1}{2} u_\tau(\mathbf{x}) + \int_{\partial\Omega} u_\tau(\mathbf{y}) \mathbf{K}(\mathbf{x} - \mathbf{y}) \cdot \boldsymbol{\tau}(\mathbf{x})\, \mathrm{d}s(\mathbf{y}) = \int_{\partial\Omega} u_n(\mathbf{x}) \mathbf{K}^\perp(\mathbf{x} - \mathbf{y}) \cdot \boldsymbol{\tau}(\mathbf{x})\, \mathrm{d}s(\mathbf{y})$$

$$+ \iint_\Omega \omega(\mathbf{y}) \mathbf{K}(\mathbf{x} - \mathbf{y}) \cdot \boldsymbol{\tau}\ (\mathbf{x})\, \mathrm{d}\Omega(\mathbf{y}). \tag{13}$$

Associated with the tangential velocity at the boundary is a circulation density γ on the boundary. It is given by the jump of the tangential velocity from the value given by equation (13) to a prescribed value just outside the computational domain.

The closed boundary of the computational domain is discretized by a set of N_p straight panels, each having a uniform source density q and circulation density γ. Across such a panel the normal and the tangential component of the velocity jump by an amount of q and γ, respectively. In case one chooses the velocity outside the fluid domain to be zero, the boundary condition of zero normal velocity at solid walls requires a zero source strength, while at the parts of the boundary where there is an in- or outflow the source strength is specified equal to the in- or outflow. The Dirichlet condition (velocity potential is specified) is used on the boundary to determine the circulation density on each panel. It is implemented by imposing a zero tangential velocity on the non-fluid side of the boundary, i.e., in discretized form at each panel midpoint. The discretized equation representing the Dirichlet boundary condition has the form

$$\frac{1}{2}\gamma_j + \sum_{k=1, k\neq j}^{N_p} \gamma_k K_\gamma(j,k) + \sum_{k=1, k\neq j}^{N_p} q_k K_q(j,k) + \sum_{k=1}^{N} \Gamma_k K_\Gamma(j,k) = 0, \quad \text{for } j = 1, \ldots, N_p, \tag{14}$$

where $K(j,k)$ are the aerodynamic influence coefficients which determine the influence of the source (K_q) or the surface vortex distribution (K_γ) of the kth panel (or the influence of the kth point vortex (K_Γ)) exercised at the midpoint of the jth panel. For non-moving solid boundaries $K_q(j,k)$ and $K_\gamma(j,k)$ depend only on the fixed geometry of the computational

domain and are independent of time. $K_\Gamma(j,k)$, however, is time-dependent since the vortex blobs are advected with the flow. In the case of straight panels with uniform source and surface vortex distributions the aerodynamic influence coefficients can be written as

$$K_\gamma(j,k) = \int_{s_k} \mathbf{K}(\mathbf{x}_j - \mathbf{x}_k)\cdot\boldsymbol{\tau}_j \,\mathrm{d}s,$$

$$K_q(j,k) = -\int_{s_k} \mathbf{K}^\perp(\mathbf{x}_j - \mathbf{x}_k)\cdot\boldsymbol{\tau}_j \,\mathrm{d}s, \qquad K_\Gamma(j,k) = \mathbf{K}(\mathbf{x}_j - \mathbf{x}_k)\cdot\boldsymbol{\tau}_j. \tag{15}$$

In these equations s denotes the arc length along a panel and s_k is the part of the boundary belonging to the kth panel. Note that for the implementation of the boundary condition the original singular kernel for the vortex blobs is used. When this is not done, the solution loses any physical meaning. For every time step the surface vortex distribution on the boundary can be solved by using an algorithm based on an LU-decomposition. When the circulation density is known the vortex blobs can be advanced in time by integrating equation (7). This equation is integrated in time by using a fourth order Runge–Kutta scheme.

The method described in this section solves the vorticity–transport equation for inviscid flow but does not include any means to generate vorticity. If this method is to be applied to separating flows a mechanism for generating vorticity is needed. For flow separation from sharp edges, as shown in Figure 2, simplified models are available. These models have this in common that they can be considered as an implementation of an approximate Kutta condition at the sharp edge. The method used here is described below.

When a two-dimensional flow is separating from a wall, the vorticity that was previously in the boundary layer is transported with a certain transport velocity into the main flow domain. In the present model the vorticity of the boundary layer is concentrated in the circulation density on the solid walls, which is equal to the tangential (slip) velocity at the walls. The total amount of vorticity that is released into the domain per unit time is then the product of the transport velocity and the vorticity in the boundary layer. In this method at a sharp corner this process can be modelled as shown in Figure 2.

A new vortex blob is generated at an initial position determined by the velocity at the midpoints of the two corner panels,

$$\mathbf{x}_{init} = \mathbf{x}_{corner} + \tfrac{1}{2}(\mathbf{u}_i + \mathbf{u}_{i+1})\Delta t,$$

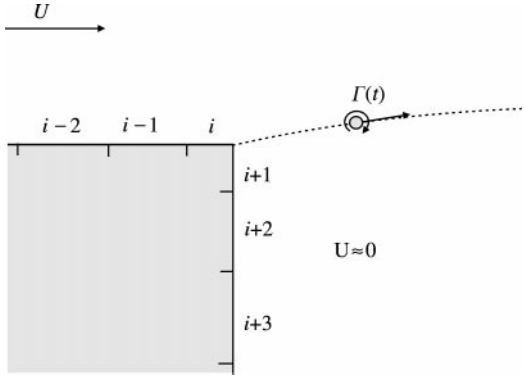

Figure 2. Close-up of the numerical model of the flow separation over a downward facing step, specifically the generation of a new vortex.

where Δt is the time step. The constant $\frac{1}{2}$ in this equation is rather arbitrary. Results are fortunately not sensitive to this choice [7]. From this initial position onwards the nascent vortex blob is transported with the local flow velocity. The circulation of the nascent vortex blob is growing until a new vortex is generated. The change of the shear-layer circulation is determined by

$$\mathrm{d}\Gamma/\mathrm{d}t = -\tfrac{1}{2}|\mathbf{u}_i + \mathbf{u}_{i+1}|(\mathbf{u}_i \cdot \boldsymbol{\tau}_i + \mathbf{u}_{i+1} \cdot \boldsymbol{\tau}_{i+1}).$$

In this equation the transport velocity is represented by the term $\frac{1}{2}(\mathbf{u}_i + \mathbf{u}_{i+1})$, which is the average of the velocities at the midpoints of the two corner panels. The amount of vorticity that is transported into the flow domain is the average of the circulation density on the two corner panels. Although this is a very simple approximation of a complex process it is very robust, leading to a very reasonable description of flow separation at sharp edges as the results will confirm. As the interaction between the acoustic and vortical fields is strongest near sharp edges where flow separation occurs, the accuracy of the prediction of the model is largely determined by the accuracy of the implementation of the Kutta condition.

3. INTEGRAL REPRESENTATION FOR THE PRESSURE

A natural way of computing the pressure field for an incompressible flow starting from a known vorticity distribution and boundary conditions is now presented. The adoption of an integral representation leads to a more accurate evaluation of the solution than a direct numerical integration along the boundary of the tangential projection of the momentum equation (Navier–Stokes or Euler, according to the nature of the flow). Moreover, the deduction to be presented can suggest a quite straightforward application to acoustic problems.

In the framework of vortex methods for incompressible flows it is common to ignore the pressure field for two main reasons. Firstly, to solve the momentum equations written in terms of vorticity, knowledge of the pressure distribution is not needed, since p and ω are decoupled variables. The vorticity does not depend directly on the pressure; meanwhile p is explicitly determined by the dynamics of ω. Secondly, the total load acting on a surface (both for internal or external flow problems) can easily be obtained in terms of the time variation of the vortex impulse [16].

The dynamics of incompressible flows are governed by the conservation of mass and the conservation of momentum as presented in equation (2). The boundary conditions are the no-slip velocity on solid walls and an imposed uniform inlet velocity profile. Therefore $\mathbf{u} = (0, 0)$ on solid walls and $u_n = -u_{in}(t)$, $u_\tau = 0$ at the inlet section. Here u_n and u_τ represent the normal projection and the tangential projection of the velocity vector with respect to the wall respectively. Note that the unit normal vector $\mathbf{n}$ is directed outwards and because u_{in} is the inflow velocity, the minus sign on the right-hand side appears. As explained earlier, the computational domain consists also of a far outlet section for which, $u_n = u_e(t)$, $u_\tau = 0$, where $u_e(t)$ is the uniform exit velocity that is evaluated by applying the conservation of mass. This is strictly true only if the outlet section is really at infinity. Nevertheless, the asymptotic behavior of the perturbation velocity is a dipole-like one; hence the dependency of the solution on this approximation may be easily relaxed by choosing a boundary sufficiently far downstream. The unit tangential vector $\boldsymbol{\tau}$ along the boundary is defined in an anti-clockwise direction (leaving the fluid domain on the left), while the normal one is directed outwards of the domain, so that $\mathbf{n}^\perp = \boldsymbol{\tau}$ as is shown in Figure 1.

If the divergence operator is applied to equation (2) a Poisson differential equation is obtained for the non-dimensionalized total pressure $P = p + |u|^2/2$:

$$\nabla^2 P = -\nabla\cdot(\omega\mathbf{u}^\perp). \tag{16}$$

The boundary conditions for P have to be chosen according to those for the velocity field. This means that the dynamic boundary condition for P is provided by the normal projection of the Navier–Stokes equations:

$$\mathbf{n}\cdot\nabla P = -\frac{\partial u_n}{\partial t} - \omega u_\tau + \frac{1}{\mathrm{Re}}\,\boldsymbol{\tau}\cdot\nabla\omega.$$

Therefore, P appears to be the solution of an inner Neumann problem, which admits a non-unique solution. This is consistent with the physical definition of the pressure and so P will be correctly found by subtracting a particular solution independent of the boundary conditions ($P =$ constant).

A straightforward application of Green's second identity provides an integral representation for the total pressure,

$$c(\mathbf{x})P(\mathbf{x}) = -\iint_\Omega \nabla_y\cdot(\omega\mathbf{u}^\perp)G(\mathbf{x}-\mathbf{y})\,\mathrm{d}\Omega(\mathbf{y}) - \int_{\partial\Omega} P(\mathbf{y})\boldsymbol{\tau}\cdot\mathbf{K}(\mathbf{x}-\mathbf{y})\,\mathrm{d}s(\mathbf{y}) - \int_{\partial\Omega}\frac{\partial P(\mathbf{y})}{\partial n}G(\mathbf{x}-\mathbf{y})\,\mathrm{d}s(\mathbf{y}),$$

where $\mathbf{y}$ is the integration variable, Ω is the two-dimensional control area, $\partial\Omega$ is the closed curve enclosing the control area, and $\mathrm{d}s$ denotes integrating along the curve $\partial\Omega$. The coefficient $c(\mathbf{x})$ is equal to $\frac{1}{2}$ or 1 as the point $\mathbf{x}$ is on the fluid side of the boundary or in the fluid domain, respectively; $G(\mathbf{x}-\mathbf{y})$ is the free space Green function for the Laplace problem, given by

$$G(\mathbf{x}) = \frac{1}{2\pi}\log|\mathbf{x}|, \quad \mathbf{x}\in R^2,$$

and $\mathbf{K}(\mathbf{x}-\mathbf{y}) = -\nabla_y^\perp G(\mathbf{x}-\mathbf{y})$ is the Biot–Savart kernel,

$$\mathbf{K}(\mathbf{x}) = \frac{1}{2\pi}\frac{\mathbf{x}^\perp}{|\mathbf{x}|^2}, \quad \mathbf{x}^\perp = (-x_2, x_1).$$

Integrating the previous expression by parts and taking into account the boundary condition one finds

$$c(\mathbf{x})P(\mathbf{x}) = \iint_\Omega \omega\mathbf{u}\cdot\mathbf{K}(\mathbf{x}-\mathbf{y})\,\mathrm{d}\Omega(\mathbf{y}) + \int_{\partial\Omega}\omega u_\tau G(\mathbf{x}-\mathbf{y})\,\mathrm{d}s(\mathbf{y}) - \int_{\partial\Omega} P(\mathbf{y})\boldsymbol{\tau}\cdot\mathbf{K}(\mathbf{x}-\mathbf{y})\,\mathrm{d}s(\mathbf{y}) + \int_{\partial\Omega}\frac{\partial u_n}{\partial t}G(\mathbf{x}-\mathbf{y})\,\mathrm{d}s(\mathbf{y}) - \int_{\partial\Omega}\omega u_\tau G(\mathbf{x}-\mathbf{y})\,\mathrm{d}s(\mathbf{y}) + \int_{\partial\Omega}\frac{1}{\mathrm{Re}}\frac{\partial\omega}{\partial s}G(\mathbf{x}-\mathbf{y})\,\mathrm{d}s(\mathbf{y}).$$

Moreover, one can consider, for $\mathbf{y} \in \partial\Omega$, the following identity:

$$G(\mathbf{x}-\mathbf{y})\frac{\partial\omega}{\partial s} = \frac{\partial}{\partial s}[G(\mathbf{x}-\mathbf{y})\omega] - \omega\mathbf{n}\cdot\mathbf{K}(\mathbf{x}-\mathbf{y}).$$

The contour $\partial\Omega$ is a closed curve and the functions $G(\mathbf{x}-\mathbf{y})$ and ω are single-valued on it; hence the integral of the first term on the right-hand side will drop out. The solution of the problem (16) is then expressed in terms of an integral representation, valid for $\mathbf{x} \in \partial\Omega$ or $\mathbf{x} \in \Omega$:

$$c(\mathbf{x})P(\mathbf{x}) = \iint_{\Omega} \omega\mathbf{u}\cdot\mathbf{K}(\mathbf{x}-\mathbf{y})\,\mathrm{d}\Omega(\mathbf{y}) - \int_{\partial\Omega} P(\mathbf{y})\boldsymbol{\tau}\cdot\mathbf{K}(\mathbf{x}-\mathbf{y})\,\mathrm{d}s(\mathbf{y})$$
$$+ \int_{\partial\Omega} \frac{\partial u_n}{\partial t} G(\mathbf{x}-\mathbf{y})\,\mathrm{d}s(\mathbf{y}) - \int_{\partial\Omega} \frac{1}{\mathrm{Re}}\,\omega\mathbf{n}\cdot\mathbf{K}(\mathbf{x}-\mathbf{y})\,\mathrm{d}s(\mathbf{y}). \tag{17}$$

As mentioned before, for $\mathbf{x} \in \partial\Omega$ the constant $c(\mathbf{x})$ is equal to $\frac{1}{2}$ and the relation (17) gives rise to the following boundary integral equation of the second kind:

$$\frac{1}{2}P(\mathbf{x}) + \int_{\partial\Omega} P(\mathbf{y})\boldsymbol{\tau}\cdot\mathbf{K}(\mathbf{x}-\mathbf{y})\,\mathrm{d}s(\mathbf{y}) = \iint_{\Omega} \omega\mathbf{u}\cdot\mathbf{K}(\mathbf{x}-\mathbf{y})\,\mathrm{d}\Omega(\mathbf{y}) + \int_{\partial\Omega} \frac{\partial u_n}{\partial t} G(\mathbf{x}-\mathbf{y})\,\mathrm{d}s(\mathbf{y})$$
$$- \int_{\partial\Omega} \frac{1}{\mathrm{Re}}\,\omega\mathbf{n}\cdot\mathbf{K}(\mathbf{x}-\mathbf{y})\,\mathrm{d}s(\mathbf{y}). \tag{18}$$

As a result of the adoption of a Neumann boundary condition, only the pressure distribution is unknown, which is obtained by imposing in a discretized fashion the integral equation at a number of collocation points. The boundary of the geometry $\partial\Omega$ is approximated by straight elements (panels) carrying a panel-wise uniform distribution of P (for a first order scheme).

Note that the discretized form of equation (18) leads to an algebraic system of linear equations. The square matrix of coefficients is singular, with one eigenvalue equal to zero (i.e. its rank is equal to $N-1$). Therefore, the solution of equation (18) should be obtained by applying a singular-value-decomposition (SVD) technique for the inversion of the matrix, and then selecting the solution by subtracting the reference farfield value of the total pressure P_∞: the numerical technique needed for solving equation (18) reflects exactly the non-uniqueness property of the pressure field. However, we found that the problem can be transformed to a non-singular one simply by replacing the equation at one of the collocation points with the condition $P = P_{ref}$ at some point on the boundary. This technique leads to a solution consistent and equal to that obtained with an SVD procedure, with the main advantage of a simpler and faster algorithm based on an LU decomposition of the coefficients matrix.

4. NUMERICAL RESULTS

4.1. GENERAL RESULTS

By varying the value of the desingularization parameter δ_v in the range of 0·05 to 0·2 the stability and accuracy of the numerical method has been analyzed. Since the time step must reduce approximately proportional to the value of δ_v for a stable numerical solution, the

number of point vortices increases inversely proportional to δ_v. It was found that for values of $\delta_v < 0{\cdot}2$ the condition of tangential flow separation from the sharp edge of the diaphragm is quite well satisfied. Therefore, in order to have a stable numerical method for a reasonable choice of the time step (in view of the computational effort), the value of the desingularization parameter δ_v is chosen equal to 0·1 times the height of the aperture of the diaphragm h_d. This value of δ_v will yield numerical results that are accurate enough for our purposes.

Uniform flow conditions are imposed on the in- and outflow boundary. The in- and outflow velocities consist of a steady flow component and an oscillating flow that is superimposed,

$$u_1(t^*) = u_2(t^*) = u_1 + u_1' \sin(2\pi \,\mathrm{Sr}\, t^*),$$

where t^* is the time non-dimensionalized with the reference length h_d and the reference velocity $u_d = (S_v/S_d)u_1$. The numerical simulation is started from a steady potential-flow solution.

The diaphragm that has been used in the experiments (diaphragm II shown in Figure 3) is approximated by one of the two-dimensional forms shown in Figure 4. The numerical simulations were performed for two different geometries of the diaphragm. First a thin diaphragm was used that is a representation of a diaphragm of infinitesimal thickness in the vortex-blob method. It has a thickness much smaller than the height h_d of the aperture of the diaphragm: its thickness is $0{\cdot}05h_d$. The second diaphragm has a thickness that is of the same order as the height h_d of the aperture. This is the diaphragm that is actually used in the experiments. It has a thickness equal to $0{\cdot}63h_d$. The ratio of pipe cross-sectional area and the aperture of the diaphragm is 0·27 and this corresponds in the experiments to $h_d = 6{\cdot}4$ mm in both cases.

In Figure 5, a typical result of the vortex-blob method is shown for an amplitude of the fluctuating velocity $u_{ac} = u_1'/u_1 = 0{\cdot}1$. Top to bottom time increases with a quarter period of oscillation $T/4$ between each figure. The simulation exhibits features that are well known

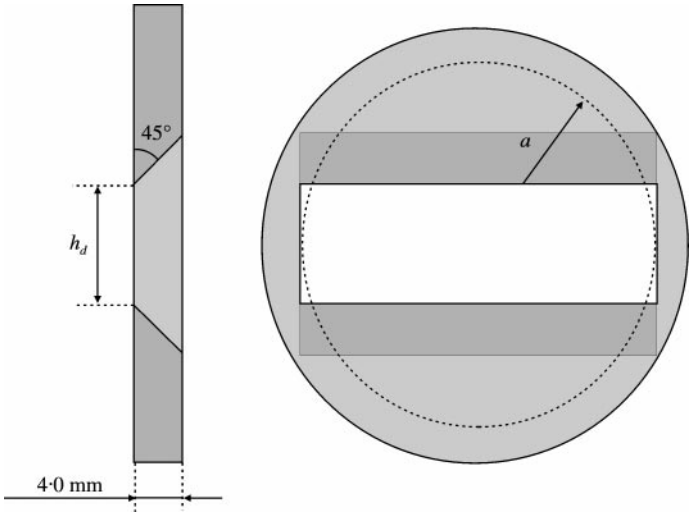

Figure 3. Three different slit-like diaphragms that have been used in the experiments: diaphragm I has $h_d = 10{\cdot}7$ mm and $S_d/S_p = 0{\cdot}45$; diaphragm II has $h_d = 6{\cdot}4$ mm and $S_d/S_p = 0{\cdot}27$; diaphragm III has $h_d = 2{\cdot}6$ mm and $S_d/S_p = 0{\cdot}11$.

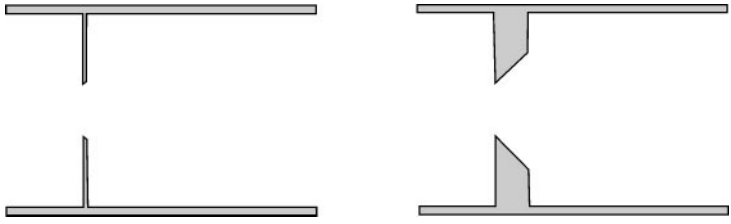

Figure 4. The two diaphragms that have been studied numerically. On the left is the thin diaphragm which is an approximation of a line diaphragm and on the right is a two-dimensional representation of the actual diaphragm used in experiments.

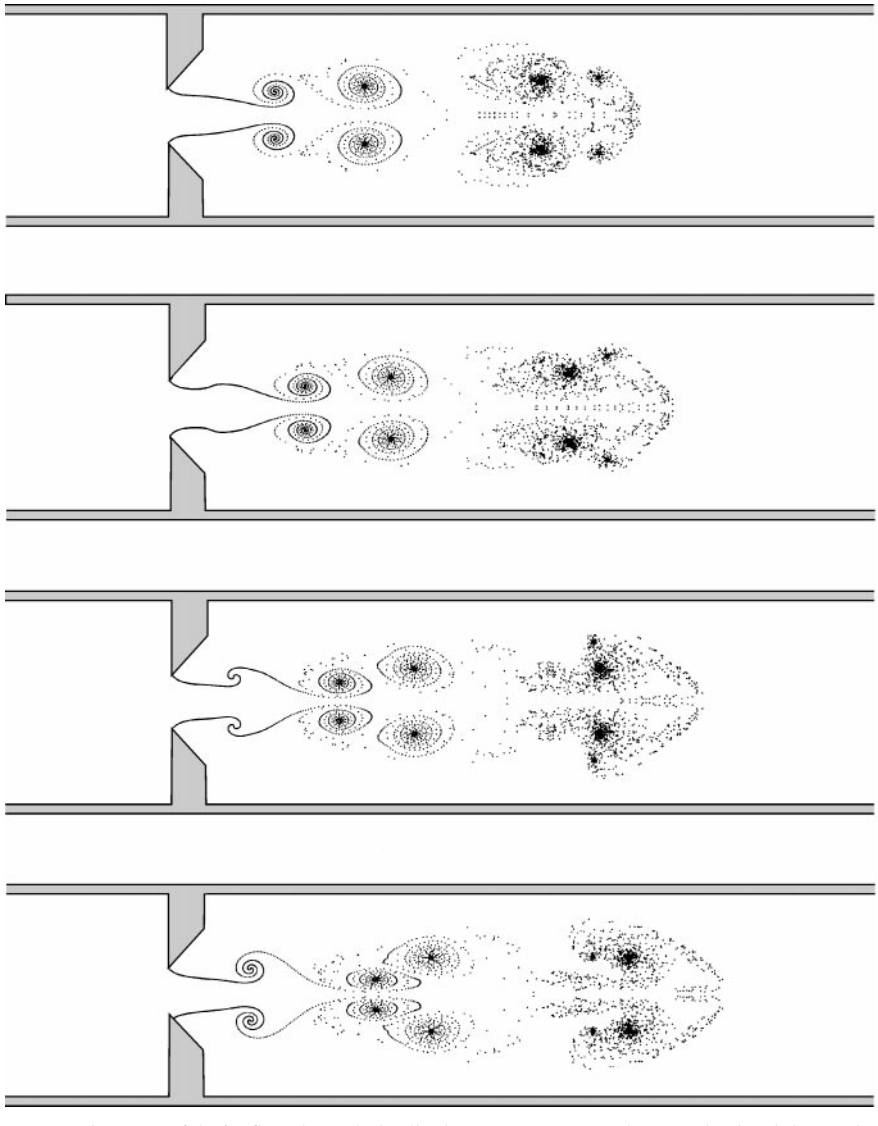

Figure 5. Development of the jet flow through the diaphragm. From top to bottom the time is increasing by $T/4$ between each figure. The markers give the positions of the point vortices. This is a result of the vortex-blob method for $\mathrm{Sr} = 0{\cdot}4$ and $u_{ac} = u_1'/u_1 = 0{\cdot}1$.

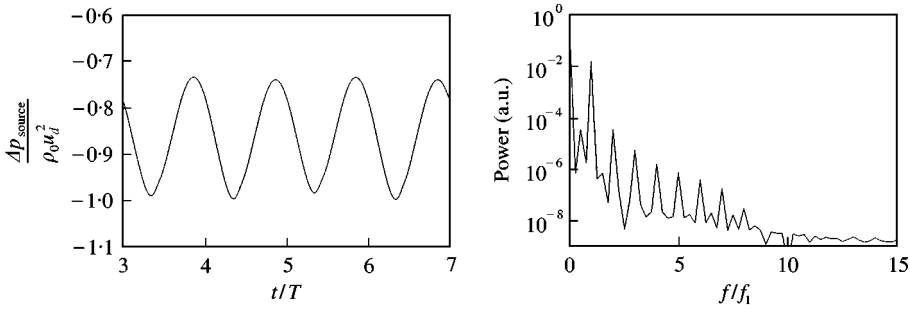

Figure 6. Acoustic source pressure (vortex pressure) as a function of time and the associated power spectrum. The simulation was started at $t = 0$. Sr = 0·4, $u_{ac} = u_1'/u_1 = 0{\cdot}1$.

for (two-dimensional) jet flows: the vena contracta effect and pairing of vortices. Although the jet flow is still developing and the flow does not look periodic, the resulting acoustic source pressure and therefore also the acoustic source power becomes periodic within three to four periods of oscillation. The acoustic source pressure (vortex pressure Δp_{source}) is shown as a function of time on the left in Figure 6. On the right the associated power spectrum is shown. The fundamental (forcing) frequency f_1 is dominant by three orders of magnitude, but several higher modes are significant. The vortex pairing visible in Figure 5 produces a period doubling relative to the fundamental period of forcing. This mode at $\frac{1}{2}f_1$ is also weakly present in the signal as can be seen in the power spectrum. Further numerical simulation indicates that for $\mathrm{Sr} \geqslant 0{\cdot}5$ the period doubling has a maximum influence on the signal. The acoustic results for the fundamental frequency appear not to be sensitive to the ratio $u_{ac} = u_1'/u_1$ up to a value of 0·1. This allows one to compare the results with those of low-amplitude experiments.

4.2. ACOUSTIC SOURCE POWER

In an unsteady vortical flow the interaction of the acoustic field with the vorticity field can lead to production or dissipation of acoustic energy. Howe [5, 17] proposed an energy formulation for the acoustic power generated by a turbulent flow. The amount of acoustic energy that is generated or dissipated in the numerical simulations is obtained by two methods. The first method is a direct implementation of Howe's energy formulation for the time-averaged acoustic source power as used by Kriesels *et al.* [8],

$$\langle \mathscr{P} \rangle = -\rho_0 \int_V \langle (\boldsymbol{\omega} \times \mathbf{u}) \cdot \mathbf{u} \rangle \, \mathrm{d}V, \tag{19}$$

where $\boldsymbol{\omega} = \nabla \times \mathbf{u}$ is the vorticity, $\mathbf{u}$ is the convection (total) velocity of the vorticity, and $\mathbf{u}'$ is the acoustic velocity defined as the irrotational time-dependent part of the velocity. V is a volume enclosing the vorticity present in the flow field. The second method is the integral pressure formulation of section 3 using the Green function,

$$\langle \mathscr{P} \rangle = \int_S \langle \mathbf{I} \cdot \mathbf{n} \rangle \, \mathrm{d}S, \tag{20}$$

where $\mathbf{I} = B'(\rho \mathbf{u})'$, and B' is the total-enthalpy perturbation. S is the surface enclosing the whole computational domain. In the limit of incompressible flow this can be approximated

by $\mathbf{I} = p'\mathbf{u}'$. Since the boundaries are chosen to be far from the region of vorticity, the in- and outflow velocity can be considered uniform. In that case the integral reduces to the time average of the pressure difference due to the presence of vorticity times the acoustic velocity u_1' at the boundaries,

$$\langle \mathscr{P} \rangle = S_p \langle \Delta p_{source} u_1' \rangle, \tag{21}$$

where Δp_{source} is defined as the difference between the actual pressure p in the flow containing vorticity and the potential-flow contribution p_{pot} to the actual pressure:

$$\Delta p_{source} = \Delta p(t) - \Delta p_{pot}(t). \tag{22}$$

For compact sources at low Mach number, results of equation (21) should be equivalent to results of Howe's formulation (19). Differences in the results of these two formulations are due to numerical errors and therefore a measure for the numerical accuracy.

In Figure 7 the time-averaged acoustic source power is shown as a function of the Strouhal number ($\mathrm{Sr} = f h_d/u_d$). The power is non-dimensionalized with the diaphragm velocity $u_d = S_p/S_d u_1$ and the cross-sectional area of the aperture S_d. These results have been obtained for the thick ($0{\cdot}63 h_d$) diaphragm. Clearly, this diaphragm is only dissipating acoustic energy. In the figure the results of both formulations (19) and (21) are presented. The two formulations are in fair agreement, which is a measure for the accuracy of the vortex-blob results. At $\mathrm{Sr} = 0$ the quasi-steady incompressible-flow model of Hofmans *et al.* [1] is used. The results of the vortex-blob method show a quasi-steady limit that approaches this result reasonably well. The difference in the calculated power is only 7%. The quasi-steady limit of the numerical simulations differs from the quasi-steady model due to the inability of the vortex-blob method to capture accurately the vena contracta effect (within 5%) using the current numerical input parameters. For Sr larger than 0·5 a slight oscillation in the power can be seen in Figure 7. A satisfactory explanation is not yet found for this feature. This could be a "whistling" effect of the diaphragm (see the papers of Hirschberg [18] and Peters [7]).

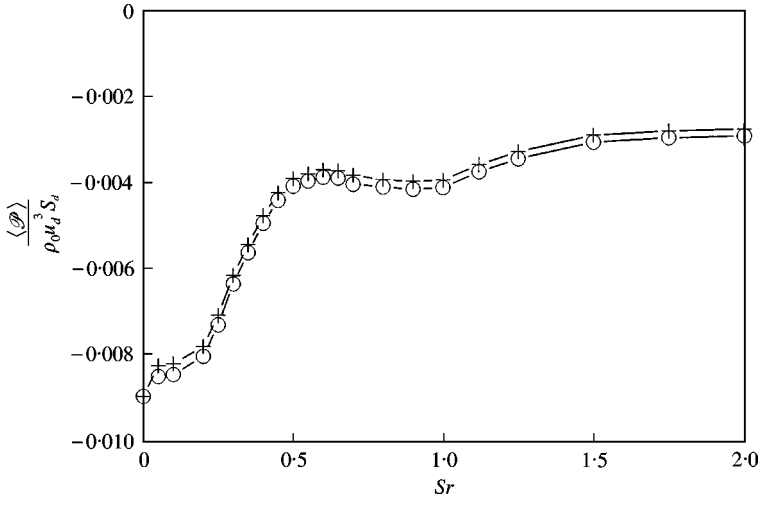

Figure 7. Time-averaged acoustic source power as a function of Strouhal number for a slit-like diaphragm in a pipe. The slit area is 27% of the pipe area and $u_{ac} = u_1'/u_1 = 0{\cdot}1$. Results obtained by Howe's formulation are marked by + and results obtained by the integral pressure formulation are marked by ○.

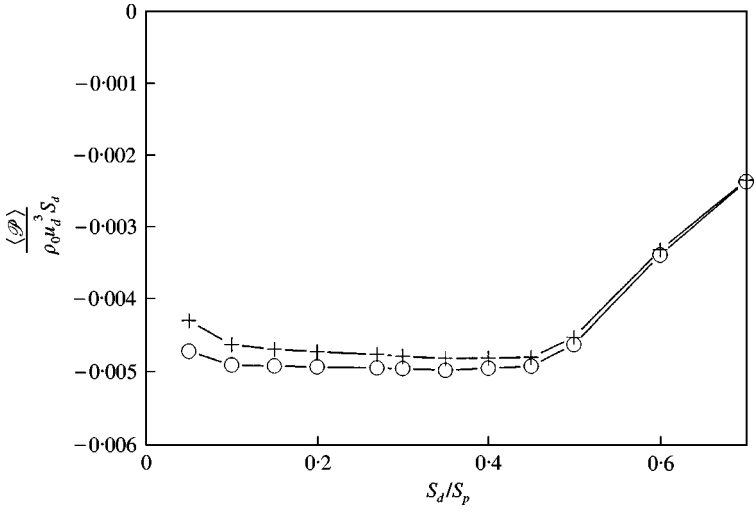

Figure 8. Time-averaged acoustic source power as a function of the ratio of the cross-sectional area of the aperture and the cross-sectional area of the pipe, a slit-shaped diaphragm in a pipe: Sr = 0·4, $u_1'/u_1 = 0{\cdot}1$. Results obtained by Howe's formulation are marked by + and results obtained by the pressure formulation are marked by ○.

In order to illustrate the influence of the pipe wall on the acoustic behavior of the diaphragm the time-averaged acoustic source power is presented in Figure 8 as a function of the relative aperture of the diaphragm S_d/S_p. For small values of this ratio the power reaches a constant value. Only when the ratio S_d/S_p exceeds 0·45 is the power significantly influenced by the geometry. At very low values ($<0{\cdot}1$) the power starts to deviate from the constant value but this is most likely due to inaccuracies in the numerical method for these geometries. This is also indicated by the divergence between the results of Howe's formulation and those of the pressure formulation for small values of S_d/S_p. This divergence can be explained by a difference in sensitivity of the two prediction methods to the flow near the separation point. It also indicates that the flow near this separation point is crucial for the aeroacoustic response of the diaphragm. This confirms our conclusions from our companion paper that the description of the turbulent mixing region downstream of the jet is not critical.

4.3. ACOUSTIC RESPONSE

In order to interpret the numerical results acoustically, an acoustic model must be used. The first equation is the incompressible form of the equation of mass conservation across the acoustic source region,

$$p_1^+ - p_1^- - (p_2^+ - p_2^-) = 0, \tag{23}$$

where region 1 is the region upstream of the diaphragm and region 2 is the region downstream of the diaphragm. The second equation follows from the momentum conservation across the acoustic source region upon neglecting friction,

$$p_1^+ + p_1^- - (p_2^+ + p_2^-) = \Delta p_{source} + \mathrm{i}\rho_0 \omega L_{\mathrm{eff}} u_1', \tag{24}$$

where Δp_{source} is the acoustic source pressure obtained from numerical simulations and $i\omega L_{\text{eff}}$ is the contribution due to the inertial effects of the potential flow through the diaphragm. This separation of contributions is due to the definition of Δp_{source} which does not include potential-flow contributions that influence the acoustic inertance of the diaphragm. In the case of the diaphragm considered here (diaphragm II, $S_d/S_p = 0{\cdot}27$) the effective length L_{eff} is $2{\cdot}59h_d$ obtained from the potential-flow solution.

In Figure 9 the acoustic source pressure is shown as a function of the acoustic amplitude for the thick diaphragm at Sr = 0·4. For $u_1'/u_1 < 0{\cdot}1$ the acoustic source pressure appears to be linearly proportional to the acoustic velocity u_1'. If one assumes the acoustic source pressure to be proportional to the acoustic velocity u_1' one obtains the equation

$$(p_1^+ + p_1^-) - (p_2^+ + p_2^-) = Ku_1' + i\rho_0\omega L_{\text{eff}}u_1', \tag{25}$$

where K is a function of Sr and S_d/S_p. This can be rewritten as

$$p_1^+ + p_1^- - (p_2^+ + p_2^-) = (K + i\rho_0\omega L_{\text{eff}})\frac{p_1^+ - p_1^-}{\rho_0 c_0}. \tag{26}$$

One can now write the two equations (23) and (26) in the form of a scattering matrix [6],

$$\begin{pmatrix} p_2^+ \\ p_1^- \end{pmatrix} = \begin{pmatrix} T^+ & R^- \\ R^+ & T^- \end{pmatrix}\begin{pmatrix} p_1^+ \\ p_2^- \end{pmatrix}, \tag{27}$$

where

$$T^+ = T^- = \frac{2\rho_0 c_0}{K + i\rho_0\omega L_{\text{eff}} + 2\rho_0 c_0} \tag{28}$$

and

$$R^+ = R^- = \frac{K + i\rho_0\omega L_{\text{eff}}}{K + i\rho_0\omega L_{\text{eff}} + 2\rho_0 c_0}. \tag{29}$$

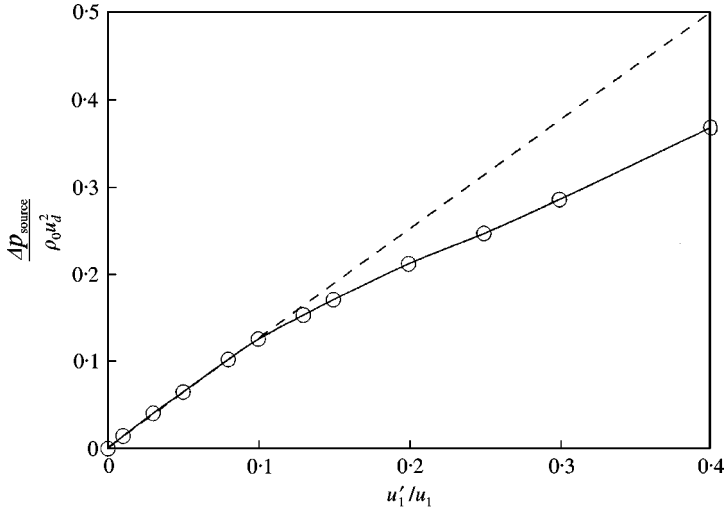

Figure 9. Acoustic source pressure as a function of the acoustic amplitude for the thick diaphragm at Sr = 0·4. Note that for small acoustic amplitudes the source pressure is linearly proportional to the acoustic amplitude.

TABLE 1

Numerical results obtained with the vortex-blob method for the acoustic source pressure and the phase difference relative to the acoustic velocity for the two diaphragms; acoustic amplitude $u_{ac} = 0{\cdot}1$

	Thin		Actual	
Sr	$\lvert \Delta p_{source} \rvert / \rho U_d^2$	$\arg(\Delta p)$	$\lvert \Delta p_{source} \rvert / \rho U_d^2$	$\arg(\Delta p)$
0·0	0·180	0	0·180	0
0·1	0·169	$-0{\cdot}032\pi$	0·172	$-0{\cdot}047\pi$
0·2	0·168	$-0{\cdot}069\pi$	0·170	$-0{\cdot}105\pi$
0·3	0·160	$-0{\cdot}113\pi$	0·149	$-0{\cdot}177\pi$
0·4	0·145	$-0{\cdot}140\pi$	0·124	$-0{\cdot}206\pi$
0·5	0·128	$-0{\cdot}146\pi$	0·098	$-0{\cdot}186\pi$
0·6	0·118	$-0{\cdot}145\pi$	0·086	$-0{\cdot}147\pi$
0·7	0·110	$-0{\cdot}141\pi$	0·087	$-0{\cdot}124\pi$
0·8	0·107	$-0{\cdot}136\pi$	0·087	$-0{\cdot}112\pi$
0·9	0·104	$-0{\cdot}130\pi$	0·087	$-0{\cdot}106\pi$
1·0	0·100	$-0{\cdot}138\pi$	0·087	$-0{\cdot}110\pi$

These elements have a form similar to the elements found for the quasi-steady incompressible-flow model [1]. Also in the case of an unsteady incompressible description of the source region a symmetric matrix is obtained with elements that satisfy the relations: $T^+ + R^+ = T^- + R^- = 1$. The symmetry $T^+ = T^-$ and $R^+ = R^-$ is the result of the incompressible flow approximation.

The acoustic source pressure Δp_{source} is obtained from the numerical simulations. The method yields the acoustic source pressure as a function of two input parameters: i.e., acoustic amplitude $u_{ac} = u_1'/u_1$ and the Strouhal number Sr. In Table 1 the numerical results are presented for both diaphragms. Using equations (28) and (29) one obtains results for the reflection coefficient and transmission coefficient as a function of Strouhal number.

5. EXPERIMENTAL RESULTS

5.1. EXPERIMENTAL SET-UP AND PROCEDURE

In order to verify the accuracy of the model, experiments have been performed at the Acoustic Laboratory of the University of Le Mans (LAUM). These experiments consisted in measuring the frequency dependence of a diaphragm in a pipe at low Mach number.

The diaphragms being studied are slit-shaped diaphragms in a cylindrical pipe (see the companion paper). Although this is a three-dimensional configuration the response of the configuration is expected to be governed by the two-dimensionality of the slit-shaped diaphragm. This makes a comparison to two-dimensional numerical simulations reasonable. Three diaphragms with varying apertures have been used. The aperture can be as large as 45, 27 or 11% of the pipe cross-sectional area. In Figure 3 one of the diaphragms is shown. The edge of the diaphragms is kept sharp (radius of curvature less than 10^{-5} m) and at the downstream side the aperture diverges with a bevel angle of 45°. This ensures a predictable vena contracta effect.

The present theoretical results are to be compared with broadband scattering matrix measurements carried out at LAUM with the two-source method [6, 19] as described by Ajello [20]. The experimental set-up at LAUM is similar to the set-up as described by

Hofmans *et al.* [1]. Two sets of six loudspeakers each positioned up- and downstream of the diaphragm are used as sources of sound. Both sides of the main pipe (entrance and exit) were manufactured to be anechoic and corrections are made for the reflections that still do occur. The reflection coefficients of these terminations were typically of the order of 0·2 for the range of frequencies used in the experiments.

On both sides of the diaphragm three pressure transducers were mounted. By alternately using the upstream and downstream loudspeaker as a source of sound the four elements of the scattering matrix as defined by equation (27) can be determined. During one experimental run the elements were measured in a short time for a range of frequencies (typically 100 frequencies from 50 to 1600 Hz). Since on both sides three microphones were used to measure two acoustic waves (p^+ and p^-) a regression technique can be used to determine the elements of the matrix with the temperature as an additional unknown quantity. The two sets of microphones were placed symmetrically with respect to the plane $x = 0$ (corresponding to the upstream face of the diaphragm). The distance between the first microphone (closest to the diaphragm) and the third microphone (furthest from the diaphragm) was 0·9715 m (accuracy 0·02 mm). The second microphone in the middle is at 0·3750 m from the first microphone. A complete description of the experimental set-up and procedure used at LAUM can be found in reference [20].

5.2. EXPERIMENTAL RESULTS FOR LOW-MACH-NUMBER UNSTEADY FLOWS

The diaphragm used in the experiments presented here is shown in Figure 3. Diaphragm II with $S_d/S_p = 0{\cdot}27$ and $h_d = 6{\cdot}4$ mm has been used. The experiments have been performed at a Mach number M_1 in the main pipe of 0·0092. The frequency range was from 20 to 1620 Hz with steps of 20 Hz. The value of the Strouhal number corresponding with these measurements ranges from 0·005 to 0·9, and the Helmholtz number ranges from 0·001 to 0·13. With these values of M_1, Sr, and He an incompressible unsteady flow model is expected to be a reasonable approximation. In Figures 10–13 a comparison between

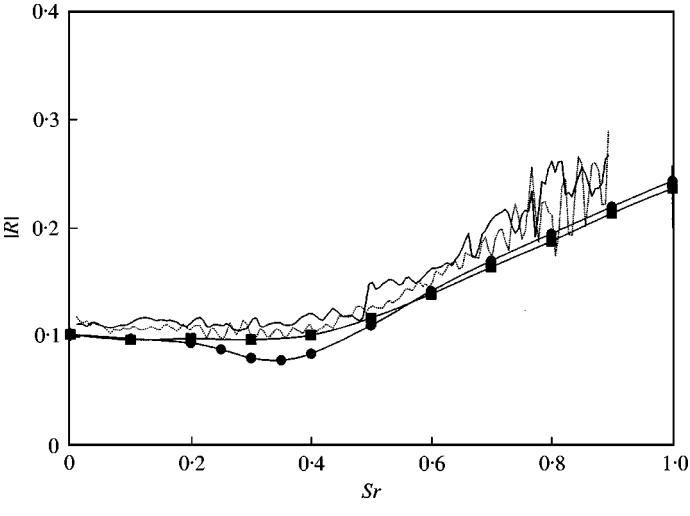

Figure 10. Comparison of measured reflection coefficients (Ajello and Auregan, 1997) and reflection coefficients obtained from the vortex-blob method. Numerical results are obtained for two different diaphragms: one with the actual thickness of 4 mm and one much thinner with a thickness of 0·32 mm: ———, $|R^+|$; ·····, $|R^-|$; ■—■, $|R|$ thin; ●—●, $|R|$ actual.

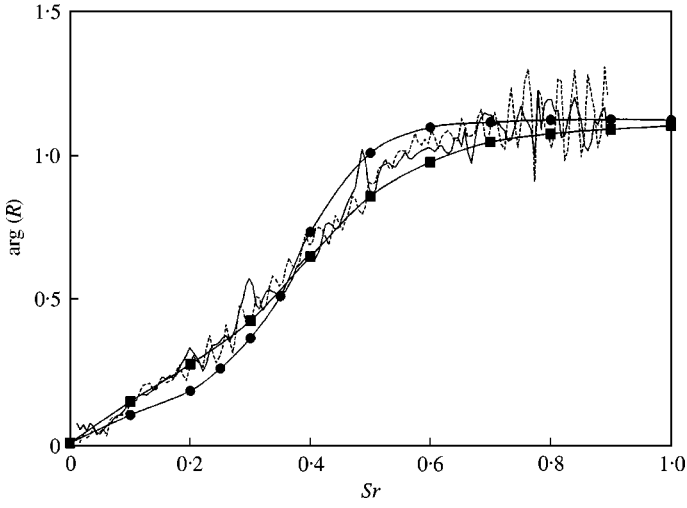

Figure 11. Comparison of measured argument of the reflection coefficients (Ajello and Auregan, 1997) and argument of reflection coefficients obtained from the vortex-blob method. Numerical results are obtained for two different diaphragms: one with the actual thickness of 4 mm and one much thinner with a thickness of 0·32 mm: ———, $\arg(R^+)$; · · · · ·, $\arg(R^-)$; ■—■, $\arg(R)$ thin; ●—●, $\arg(R)$ actual.

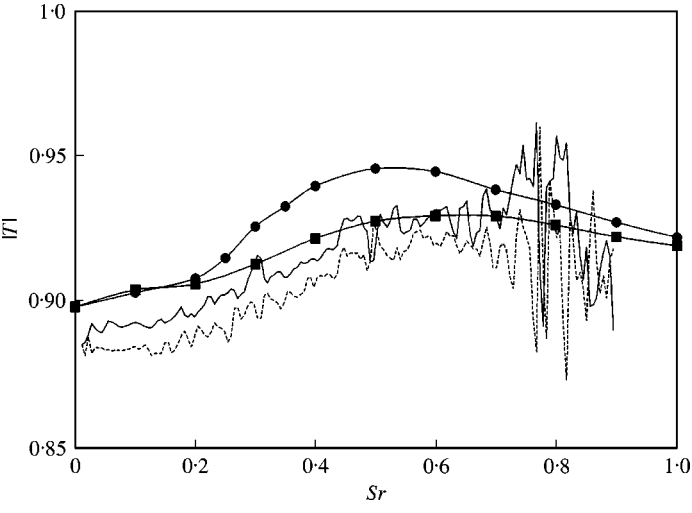

Figure 12. Comparison of measured transmission coefficients (Ajello and Auregan, 1997) and transmission coefficients obtained from the vortex-blob method. Numerical results are obtained for two different diaphragms: one with the actual thickness of 4 mm and one much thinner with a thickness of 0·32 mm: ———, $|T^+|$; · · · · ·, $|T^-|$; ■—■, $|T|$ thin; ●—●, $|T|$ actual.

experimental and numerical results is presented. The solid lines are the experimental results for R^+ and R^- or T^+ and T^-. The markers are the results obtained from the vortex-blob method for the two diaphragms of Figure 4. Since the model used to convert the numerical results for ΔP_{source} to reflection and transmission coefficients assumes incompressible flow, the scattering matrix is symmetric and only one value is found for R^+ and R^- as well as for T^+ and T^-. This is confirmed by the experimental results although the transmission

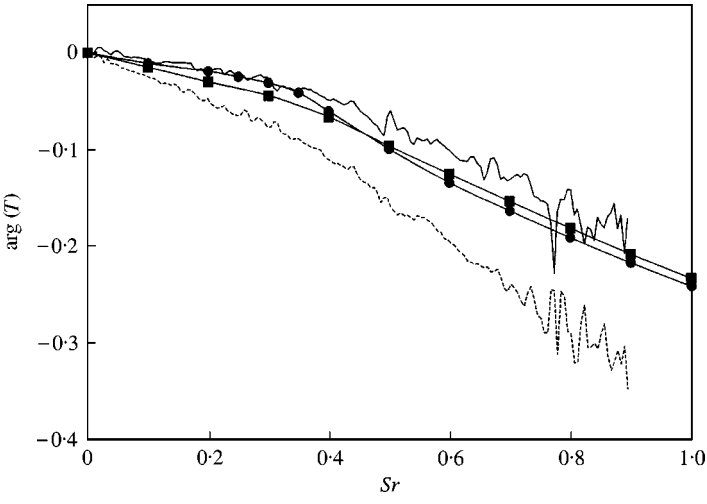

Figure 13. Comparison of measured argument of the transmission coefficients (Ajello and Auregan, 1997) and argument of transmission coefficients obtained from the vortex-blob method. Numerical results are obtained for two different diaphragms: one with the actual thickness of 4 mm and one much thinner with a thickness of 0·32 mm: ———, $\arg(T^+)$; · · · · ·, $\arg(T^-)$; ■—■, $\arg(T)$ thin; ●—●, $\arg(T)$ actual.

coefficients show a small difference between T^+ and T^-. This is most clear in Figure 13 where the phase of the transmission coefficient is shown. The difference in T^+ and T^- due to finite Mach number effects is discussed in the companion paper [1]. Furthermore, it is clear that the experimental results show a larger scatter for higher frequencies ($\mathrm{Sr} > 0{\cdot}7$) than for lower Strouhal numbers. This is most probably due to the microphone positions that are used: the set-up was designed to be used for frequencies up to 800 Hz. It is interesting to observe that the numerical results for the thin diaphragm agree better with the experimental results than the results for the thick diaphragm (actual geometry). Between $\mathrm{Sr} = 0{\cdot}2$ and $0{\cdot}6$ a small decrease in $|R|$ and a small increase in $|T|$ can be observed for the thick diaphragm. In Figure 7 an unexplained feature around $\mathrm{Sr} = 0{\cdot}5$ has already been noted. One possible explanation is that the thickness of the diaphragm introduces an additional length scale and a corresponding time scale: the jet velocity is approximately u_d/Υ and the thickness is $0{\cdot}63h_d$ so the value of the Strouhal number based on this velocity and length scale is approximately 0·38. Why this feature is absent in the experimental results is yet unclear but it may be due to the experimental set-up being essentially three-dimensional or due to viscous effects.

6. CONCLUDING REMARKS

For low-Mach-number flows that are essentially unsteady and two-dimensional the vortex-blob method can be used. Two methods are used to determine the acoustic source power numerically: Howe's energy formulation and our integral pressure formulation. Due to the implementation of these two different formulations a measure for the accuracy of the numerical results has been obtained. The pressure formulation as opposed to Howe's energy formulation contains additional information on the non-linearity of the source and can be used to predict the generation of higher harmonics.

Together with an acoustic interpretation of the flow, results of the vortex-blob method are used to predict the elements of the scattering matrix as a function of frequency. These

results are compared to results of experiments performed at LAUM and are found to be in good agreement. Surprisingly, the numerical results for a (very) thin diaphragm agree better with the experimental results than the numerical results for the geometrically more accurate representation of the actual diaphragm which is quite thick. In the vortex-blob method the thickness introduces a second length scale which results in a whistling effect at critical values of the Strouhal number. However, this effect is not observed in the experimental results. A satisfactory explanation for this is still lacking.

Finally, the vortex-blob simulations confirm that the aeroacoustic response of the diaphragm is determined locally in the region near the separation point where the free jet is formed. Both the quality of the Kutta condition imposed at the separation point and the geometry of the edge have a significant effect on the aeroacoustic response. This is in contrast with the small influence of modifications in the description of the turbulent mixing region downstream of the jet.

ACKNOWLEDGMENTS

Part of this research was sponsored by the Dutch Technology Foundation (project ETN33.2952). The vortex-blob code originally developed by A. Iafrati and G. Riccardi and modified by Peters has been used.

REFERENCES

1. G. C. J. Hofmans, R. J. J. Boot, P. P. J. M. Durrieu, Y. Auregan and A. Hirschberg 2000 *Journal of Sound and Vibration* **244**, 35–56. Aeroacoustic response of a slit-shaped diaphragm in a pipe at low Helmholtz number, 1: quasi-steady results.
2. M. S. Howe 1979 *Proceedings of the Royal Society of London, Series A* **366**, 205–223. On the theory of unsteady high Reynolds number flow through a circular aperture.
3. A. P. Dowling and I. J. Hughes 1992 *Journal of Sound and Vibration* **156**, 387–405. Absorption by a screen with a regular array of slits.
4. J. C. Wendoloski 1998 *Journal of Acoustical Society of America* **104**, 122–132. Sound absorption by an orifice plate in a flow duct.
5. M. S. Howe 1984 *IMA Journal of Applied Mathematics* **32**, 187–209. On the absorption of sound by turbulence and other hydrodynamic flows.
6. M. Abom 1991 *Mechanical Systems and Signal Processing* **5**, 89–104. Measurement of the scattering-matrix of acoustical two-ports.
7. M. C. A. M. Peters 1993 Aeroacoustical sources in internal flows. *Ph.D. Thesis, Eindhoven University of Technology*.
8. P. C. Kriesels, M. C. A. M. Peters, A. Hirschberg, A. P. J. Wijnands, A. Iafrati, G. Riccardi, R. Piva and J. C. Bruggeman 1995 *Journal of Sound and Vibration* **1 84**, 343–368. High amplitude vortex-induced pulsations in a gas transport system.
9. C. R. Anderson and C. Greengard 1985 *SIAM Journal of Statistical Computation* **22**, 413–440. On vortex methods.
10. A. L. Chorin and P. S. Bernard 1973 *Journal of Computational Physics* **13**, 423–429. Discretization of a vortex sheet, with an example of roll-up.
11. J. T. Beale and A. Majda 1985 *Journal of Computational Physics* **58**, 188–208. High order accurate vortex methods with explicit velocity kernels.
12. R. Krasny 1986 *Journal of Computational Physics* **65**, 292–313. Desingularization of periodic vortex sheet roll-up.
13. R. Krasny 1986 *Journal of Fluid Mechanics* **167**, 65–93. A study of singularity formation in a vortex sheet by the point-vortex approximation.
14. R. Krasny 1987 *Journal of Fluid Mechanics* **184**, 123–155. Computation of vortex sheet roll-up in the Trefftz plane.
15. G. C. J. Hofmans, E. A. I. van de Ven, C. F. J. den Doelder, A. Hirschberg, and A. P. J. Wijnands 1995 Unsteady flow through 2D channels with a constriction. Forum on Vortex Methods for Engineering Applications, Albuquerque.

16. P. G. SAFFMAN 1992 *Vortex Dynamics. Vortex Momentum.* New York: Cambridge University Press, Chapter 3.
17. M. S. HOWE 1980 *Journal of Sound and Vibration* **70**, 407–411. The dissipation of sound at an edge.
18. A. HIRSCHBERG, J. C. BRUGGEMAN, A. P. J. WIJNANDS and N. SMITS 1990 *Acoustica* **68**, 157–160. The whistler nozzle and horn as aero-acoustic sound sources in pipe systems.
19. M. L. MUNJAL and A. G. POIGE 1990 *Journal of Sound and Vibration* **141**, 323–333. Source location method for direct experimental evaluation of the four-pole parameters of aeroacoustic element.
20. G. AJELLO 1997 Mesures acoustiqes dans les guides d'ondes en présence d'écoulement: mise au point d'un banc de mesure applications à des discontinuités. *Ph.D. Thesis, Université du Maine.*